

# Nanoscale Quantized Oscillations in Thin-Film Growth Greatly Enhance Transconductance in Organic Transistors

Sofia Drakopoulou, Mauro Murgia, Cristiano Albonetti, Simone Benaglia, Francesco Borgatti, Michele Di Lauro, Michele Bianchi, Pierpaolo Greco, David Papo, Ricardo Garcia, Andrea Alessandrini, and Fabio Biscarini\*

**A growth mode of pentacene thin films deposited by high vacuum sublimation where the morphology versus thickness  $h$  “rings” back and forth between rough 3D films with pyramid islands and smooth 2D films with ziqqurat islands is discovered. The roughness  $\sigma$  versus  $h$  exhibits seamless coherent oscillations whose amplitude and wavelength increase as integer multiples of 1.5 ML thickness. The quantized oscillations are reconducted to dynamic wetting/dewetting transitions involving the upper layers of pentacene film. Importantly, the transconductance of organic field effect transistors, either in solid state or electrolyte-gated, exhibits antiphase oscillations with one-decade swing. Charge mobilities in the wetting regime reach  $0.1 \text{ cm}^2 \text{ V}^{-1} \text{ s}^{-1}$ , in line with high-end values reported for thin-film pentacene transistors. Controlling this growth mode enables the limitations of charge transport imposed by the roughening transition to be overcome, a universal feature of high vacuum growth to date.**

termed organic molecular beam deposition (OMBD),<sup>[6]</sup> is prototypical of nonequilibrium thin-film growth processes. Small variations of deposition parameters during deposition, such as mean thickness  $h$ , flow deposition rate  $r$ , substrate temperature  $T$ , may lead to crossover between different kinetics-controlling mechanisms, thereby resulting in a diversity of morphological features and instabilities propagating across the film.<sup>[7–10]</sup>

Molecular thin films grown in OMBD exhibit a roughening transition, from layer-by-layer (2D) to island (3D) growth.<sup>[11,12]</sup> This kinetic transition occurs at the thickness scale of a few nm, that corresponds to one to three monolayers (MLs) coverage for several molecular semiconductors,<sup>[13–16]</sup> thus

appearing a universal phenomenon of organic thin-film growth. The roughening transition critically impacts on organic thin-film transistors, as the charge carrier mobility saturates to a thickness-independent value, on the order of  $0.01 \text{ cm}^2 \text{ V}^{-1} \text{ s}^{-1}$  much lower than the values measured in pentacene single crystals  $1 \text{ cm}^2 \text{ V}^{-1} \text{ s}^{-1}$ .<sup>[17–19]</sup> Therefore, the roughening transition sets the limit to relevant properties such as the frequency response and the transconductance.

## 1. Introduction

The response of optoelectronic devices based on organic semiconductors thin films is strongly affected by their multiscale morphology.<sup>[1,2]</sup> Morphological descriptors of organic thin-film channels correlate with electronic,<sup>[3]</sup> viscoelastic,<sup>[4]</sup> and even cell adhesion properties.<sup>[5]</sup> Among thin-film deposition techniques, sublimation of molecular semiconductors in ultra-high vacuum,

S. Drakopoulou, M. Bianchi, F. Biscarini  
Dipartimento di Scienze della Vita  
Università di Modena e Reggio Emilia  
Via Campi 103, Modena 41125, Italy  
E-mail: fabio.biscarini@iit.it


S. Drakopoulou, A. Alessandrini  
Dipartimento di Fisica  
Informatica e Matematica  
Università di Modena e Reggio Emilia  
Via Campi 213/a, Modena 41125, Italy

M. Murgia, M. Di Lauro, M. Bianchi, P. Greco, D. Papo, F. Biscarini  
Center for Translational Neurophysiology  
Istituto Italiano di Tecnologia  
Via Fossato di Mortara 17–19, Ferrara 44100, Italy

M. Murgia, C. Albonetti, F. Borgatti  
CNR–ISMN  
Institute for Nanostructured Materials  
Via P. Gobetti 101, Bologna I-40129, Italy

S. Benaglia, R. Garcia  
Instituto de Ciencia de Materiales de Madrid (ICMM)  
CSIC  
Madrid 28049, Spain

P. Greco, D. Papo  
Sezione di Fisiologia Umana  
Università di Ferrara  
via Fossato di Mortara 19, Ferrara 44121, Italy

 The ORCID identification number(s) for the author(s) of this article can be found under <https://doi.org/10.1002/aelm.202300320>

© 2023 The Authors. Advanced Electronic Materials published by Wiley-VCH GmbH. This is an open access article under the terms of the Creative Commons Attribution License, which permits use, distribution and reproduction in any medium, provided the original work is properly cited.

DOI: 10.1002/aelm.202300320

The roughening transition is suitably monitored by atomic force microscopy (AFM),<sup>[11–20]</sup> X-ray reflectance, and scattering,<sup>[21,22]</sup> through the characterization of the scaling of the root mean square (rms) roughness  $\sigma$  versus  $h$ . In 2D growth, below the roughening transition,  $\sigma$  is expected to oscillate according to<sup>[13]</sup>

$$\sigma = h_0 \left[ (2n - 1) \Theta - n(n - 1) - \Theta^2 \right]^{\frac{1}{2}} \quad (1)$$

where the film thickness is related to deposition time  $t$  and coverage  $\Theta$  as  $h = r \cdot t = h_0 \cdot \Theta$ ;  $h_0$  is the height of a single layer (typically a monolayer ML; for instance, it would be  $h_0 = 1.5$  nm in pentacene and  $h_0 = 2.4$  nm in sexithienyl); the coverage  $\Theta$  is the areal fraction covered by the organic molecules expressed in monolayers MLs; the number  $n$  labels the uppermost layer growing for coverage  $\Theta$ , for instance for  $\Theta = 0.7$ ,  $n = 1$ ; for  $\Theta = 1.2$ ,  $n = 2$ . Equation (1) yields  $\sigma$  oscillations with period equal to  $h_0$  and amplitude between 0 (at integer  $\Theta = 0, 1, 2, \dots$ ) and  $h_0/2$  (at semiinteger  $\Theta = 0.5, 1.5, 2.5, \dots$ ).

Above the roughening transition occurring at time  $t_c$  and critical thickness equal to  $h_c = r t_c$ , Equation (1) no longer holds, and for  $(t - t_c)/\tau < 1$ ,  $\sigma$  scales versus time as a power law<sup>[23,24]</sup>

$$\sigma \cong \sigma_m(L) \left( \frac{t - t_c}{\tau} \right)^\beta = \sigma_m(L) \left( \frac{h - h_c}{\zeta} \right)^\beta \quad (2)$$

where  $\tau$  and  $\zeta$  are the characteristic timescale and thickness scale  $\zeta = r \cdot \tau$ ,  $\sigma_m$  is the maximum value that  $\sigma$  attains which depends on the observation length scale  $L$  when  $L < \xi$ . The characteristic length scale  $\xi$  is the correlation length, whose trend versus thickness decreases then saturates to a plateau above the transition.<sup>[5]</sup> The morphology scaling in Equation (2) denotes self-affine invariance.

For molecular semiconductors, such as pentacene and sexithienyl, the distributed growth model (DGM) reproduces the evolution of the thin-film roughness.<sup>[25,26]</sup> The roughening transition arises from a net uphill molecular flux from the bottom-most layers that becomes dominant as the Ehrlich–Schwöbel barrier at the terrace edges builds up.<sup>[13,27–29]</sup> According to DGM, the roughness oscillations of the layer-by-layer growth are rapidly damped across the transition as the power law Equation (2) sets in. A roughening transition is also predicted by other theoretical frameworks, such as the renormalization group flow equation,<sup>[30]</sup> in models of molecular beam epitaxy. Significant deviations from these ideal scaling laws occur, especially under the influence of thermally induced dewetting phenomena.<sup>[31,32]</sup>

In this article, we report a novel growth mode where pentacene film roughness  $\sigma$  exhibits seamless oscillations superimposed on the power-law scaling. Their amplitude increases versus  $h$ , instead of being damped. The correlation length oscillates in antiphase with  $\sigma$  and the roughening transition is not observed. The quantitative analysis reveals that the  $\sigma$  oscillation wavelength is quantized, instead of being constant as in 2D growth, as it increases stepwise versus  $h$  as an integer multiple (1, 2, 4) of the thickness of 1.5 ML. We reconstitute the experimental data to iterated dewetting/wetting transitions of the upper layers, whose coherence is retained across the whole range explored (more than one-decade thickness scale). Importantly, the oscillations of the morphological parameters are mirrored by oscillations of the re-

sponse of organic field effect transistors (OFETs), either in solid state or electrolyte gated. The transconductance is maximum at the wetting regime when  $\sigma$  is minimum and  $\xi$  is maximum, and the charge carrier mobility in OFETs ( $0.1 \text{ cm}^2 \text{ V}^{-1} \text{ s}^{-1}$ ) exceeds most of reported data in pentacene thin films and approaches the high-end values of pentacene single-crystal FETs, thus overcoming the limits due to the roughening transition.

## 2. Results

### 2.1. AFM Pentacene Thin-Film Morphology

In our experiment, pentacene (99%+, Merck) was sublimed in high-vacuum conditions ( $10^{-6}$  to  $10^{-7}$  mbar base pressure) in an OMBD setup. The experimental procedure is described in the Experimental Section in the Supporting Information. Importantly, the substrate temperature  $T$  during deposition was  $80^\circ\text{C}$ , a condition different from earlier pentacene growth studies where  $T$  was ranging within  $25\text{--}50$ <sup>[33]</sup> and  $120^\circ\text{C}$ .<sup>[9]</sup> Only in ref. [32] a comparable  $T = 87^\circ\text{C}$  was used for studying pentacene morphology on  $\text{SiO}_2$ . In our sample sets, film thickness  $h$  was varied from 1 to 40 nm. The morphology of pentacene thin films was studied by AFM in tapping mode in ambient conditions on 58 pentacene film samples.

The peculiar morphological evolution of pentacene thin films versus  $h$  is shown in the sequence of AFM images in **Figure 1**. At the early stages of growth (Figure 1a, 3 nm), the film exhibits fingerprint features of dewetting with monolayer-high islands coexisting with islands whose height is an integer multiple of the monolayer. At larger thicknesses (Figure 1b–o), the characteristic size and distance of the terraced structures are not monotonically varying versus increasing thicknesses. At 3 nm (Figure 1a), the film consists of 1 ML thick domains, where molecules stand in homeotropic orientation, coexisting with multilayered islands. A large fraction of bare substrate is exposed ( $\approx 30\%$ —darker regions).<sup>[34,35]</sup> Typical profiles are shown in Figure S1 in the Supporting Information and topographic images of pentacene films of different thickness grown on  $\text{SiO}_2$  at room temperature are shown in Figure S9 in the Supporting Information, for comparison.

The height distribution reveals other morphological information (**Figure 2a**): the first peak at  $\approx 0.7$  nm, ascribed to the  $\text{SiO}_2/\text{Si}$  substrate, is convolved with a small peak at  $\approx 1.4$  nm, suggesting the presence of a small population of aggregates on the  $\text{SiO}_2/\text{Si}$  substrate with molecules in the side-on configuration whose average height is  $\approx 0.7$  nm.<sup>[35,36]</sup> The third peak at  $\approx 2.5$  nm corresponds to the first monolayer of standing molecules as measured with respect to the substrate peak, i.e.,  $(1.8 \pm 0.5)$  nm, which compares to the 1.5 nm length of molecules in homeotropic configuration. The fourth peak at about 4 nm (about 1.5 nm from the third one) represents the maximum population consisting of bilayer islands. Subsequent peaks in the height distribution of Figure 2a are related to multilayered structures whose mean step height is  $1.55 \pm 0.06$  nm for three up to five monolayers. These features may be explained with coexisting 2D and 3D nucleation and subsequent growth as discussed by Verlaak et al.,<sup>[37]</sup> else by dewetting where molecules migrate from the first monolayer to form multilayered islands. This early stage dewetting might be origin of the evolution observed at the larger thicknesses.

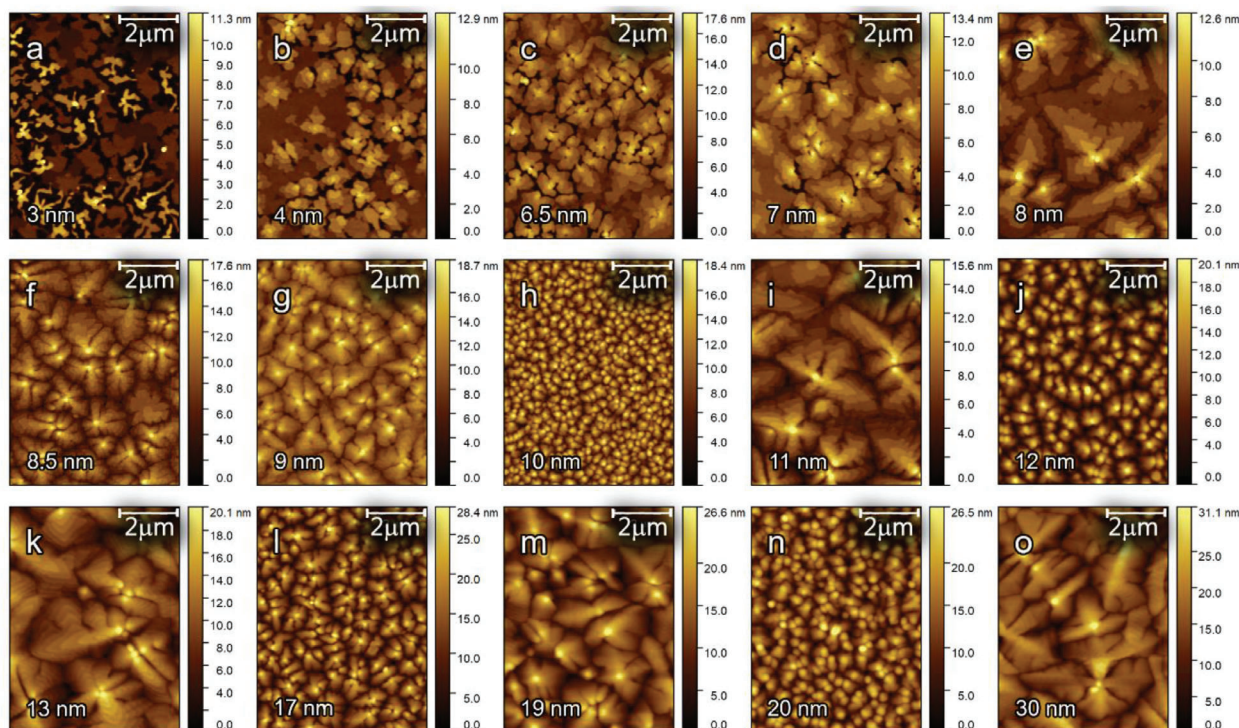


**Figure 1.** Topographic AFM images of pentacene thin films grown on  $\text{SiO}_2/\text{Si}$  substrates at  $80^\circ\text{C}$ . Film thickness is indicated on each image. Each AFM image size is  $6\ \mu\text{m} \times 8\ \mu\text{m}$  ( $307 \times 409\ \text{px}^2$ ), cropped from original  $512 \times 512\ \text{px}^2$  images.

From 4 to 7 nm (Figure 1b–d), the terraced islands are the most representative feature. The substrate is completely covered by a two MLs thick ( $2.6 \pm 0.5$ ) nm almost continuous film. On top

of it, “ziqqurat” islands with monomolecular steps (see equidistant peaks in Figure 2b) and maximum height up to the fifth ML appear. The islands of the third-to-fifth MLs increase in both area and height as thickness increases. The height distribution of 7 nm film (Figure 2c) exhibits up to eight stacked MLs.<sup>[38,39]</sup>

At 8 nm (Figure 1e), the third ML is also almost completed while islands increase their area. The characteristic height distribution of layered films with stacked monolayers is observed (Figure 2d). Remarkably, from this stage on, the films’ morphological evolution follows an unexpected trend.<sup>[33]</sup> Smaller islands with much higher density grow on the completed fourth ML (8.5 nm, Figure 1f). The height distribution (Figure 2e) shows three peaks due to the step-width reduction of the stacked monolayers (inset of Figure 2e). At 9 and 10 nm, while the average island height remains in the same range, the island density increases (Figure 2e–g). The island size decreases while the step width is further reduced before disappearing for 10 nm thick films (see insets of Figure 2e,g). This morphological evolution is accompanied by the change of “ziqqurat” islands (comb-like height distribution) into “pyramid” islands (smooth height distribution).<sup>[7,33]</sup> The same morphological evolution is repeated at larger thicknesses (Figure 1i–o).

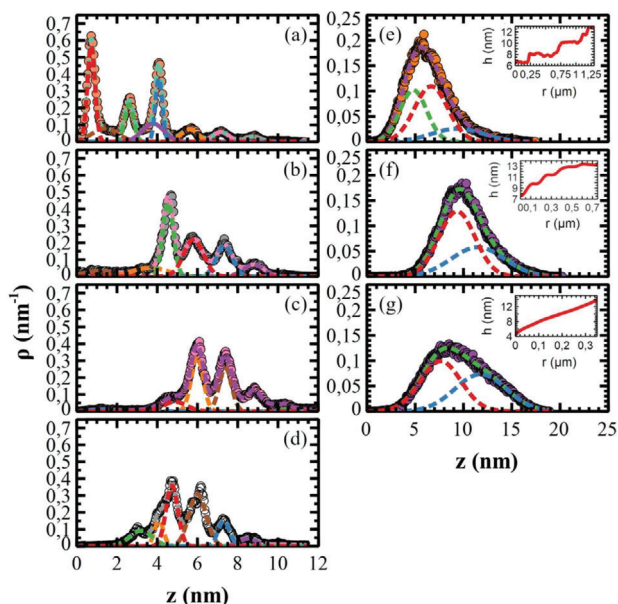


**Figure 2.** Height distribution (normalized to 1) from topographic images for pentacene thin films at some representative thickness values: a) 3, b) 4, c) 7, d) 8, e) 8.5, f) 9, and g) 10 nm. Insets: typical profiles collected along the ziqqurat and pyramid sides.

## 2.2. Scaling Analysis of Roughness and Correlation Lengths

We now analyze the surface roughness  $\sigma$  and the correlation lengths associated with the morphologies in Figure 1. The trend of  $\sigma$ , evaluated from  $10 \times 10\ \mu\text{m}^2$  images, versus  $h$  is shown in Figure 3 as black dots. The first oscillation occurs in the range 0

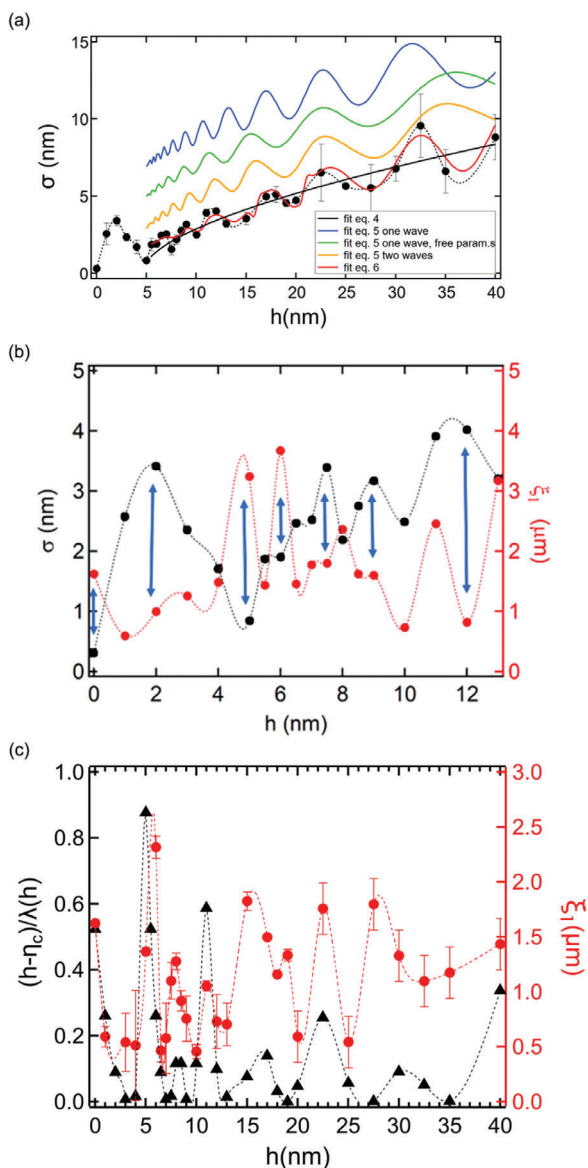


**Figure 3.** a) Evolution of rms roughness  $\sigma$  versus thickness  $h$  (black markers, error bars are standard deviations). Dotted line is guide to the eye obtained as the interpolation curve with cubic spline. Black continuous line is best fit above the transition  $h_c = 4.5$  nm to the experimental data with Equation (3). Best fit lines with Equation (4) are offset vertically for sake of clarity: blue line one wave, green line one wave and free  $a_0$  and  $\zeta$ ; orange two waves. Red line is best fit with Equation (5). b) Evolution of correlation length  $\xi_1$  versus  $h$  (red dots, right axis) at thicknesses up to 15 nm. The antiphase relation between the roughness  $\sigma$  (black markers, left axis) and  $\xi_1$  is evidenced by blue double tips. c) Angular frequency (black triangles, left axis) and correlation length  $\xi_1$  versus thickness (red dots, right axis). The red and black dotted lines are guides to the eye obtained by interpolation.

to  $\approx 5$  nm, and then increases monotonically. At first glance, the data appear scattered. We fit the data above the first oscillation (solid black line) with the stretched exponential function

$$\sigma = \sigma_0 + a_0 \cdot \left[ 1 - \exp \left[ - \left( \frac{h - h_c}{\zeta} \right)^\beta \right] \right] \quad (3)$$

that is a generalization of the power law in Equation (2) describing both the correlated fluctuations at thickness  $0 < (h - h_c) < \zeta$  and the saturation plateau for  $(h - h_c) > \zeta$ ; here  $h_c = 4.5$  nm is the thickness (here taken as the upper limit of the first oscillation whose value corresponds to a tri-layer in standing thin-film phase<sup>[40]</sup>) above which the power-law behavior starts; in our experiment the characteristic thickness  $\zeta$  lies outside our experimental thickness range (indeed, we do not observe a plateau), thus we fix it to a constant value  $\zeta = 60$  nm since we noticed that different values of  $\zeta$  do not dramatically change the exponent  $\beta$ . We also add the offset  $\sigma_0 = 0.5$  nm to account with substrate roughness. Equation (3) yields the power law Equation (2) in the limit  $h_c < h \ll \zeta$ , and saturates to the plateau  $\sigma_0 + a_0$  for  $h \gg \zeta$  (not observed in the present experiment). Best-fit exponent  $\beta = 0.73 \pm 0.06$  is comparable to the values from earlier reports (0.6–0.7). The best-fit parameters of Equation (3) reported in Table S1 in the Supporting Information are then used as fixed parameters in the forthcoming equations.

It is noticeable that all experimental values (black markers) lie above and below the black solid line Equation (3). The data interpolating line (dashed line) highlights that the data are not scattered, as oscillations interconnect the data. We count seven oscillations in the investigated range which are markedly different from those of 2D growth (described by Equation (1) and not displayed). Their wavelength (estimated as difference between thicknesses of adjacent maxima or minima) stretches as thickness increases. Peculiarly, the oscillations persist across the whole thickness range whereas the roughening transition would produce a monotonic power law.<sup>[27,28,41]</sup> Moreover, their amplitude increases, instead of damping. As expected, our attempts to fit the data with DGM<sup>[25,28]</sup> were unsuccessful (results shown in Figure S2, Supporting Information) for oscillations above the first one. To summarize, differently from the roughening transition, multiple transitions from rough (3D) to smooth (2D) morphologies occur.

To rationalize the oscillations, first we assume that they originate from the dewetting/wetting transition that is completed at  $h_c = 4.5$  nm. Oscillatory behavior of observables across a critical transition is predicted to exhibit discrete, as opposed to continuous, scale-invariance.<sup>[42]</sup> Roughness scaling should then be represented by discrete wave transforms according to equation (23) in ref. [42] with the modification described in the following. We introduce our Equation (3) as the zero-frequency component in place of the power law in equation (23) in ref. [42] to avoid diverging oscillations for increasing thickness. This leads to the following equation

$$\sigma(h) = \sigma_0 + \left[ 1 - \exp \left[ - \left( \frac{h - h_c}{\zeta} \right)^\beta \right] \right] \cdot \left[ a_0 + \sum_{m=1}^{\infty} a_m \sin \left( 2\pi \cdot m \cdot \frac{(h - h_c)}{\Lambda(h)} + \varphi_m \right) \right] \quad (4)$$

The angular frequency  $\frac{(h - h_c)}{\Lambda(h)} = \frac{\ln\{1 - \exp[-(\frac{h - h_c}{\zeta})^\beta]\}}{\ln \mu} = f_1$  depends on thickness;  $\mu$  is the scaling factor that renormalizes roughness  $\sigma(\mu h) \approx \mu^\beta \cdot \sigma(h)$ . One should

notice that for small values ( $\frac{h-h_c}{\zeta}$ ), one recovers the same expression as in equation (23) in ref. [42], viz.,  $\frac{(h-h_c)}{\Lambda(h)} \approx \left(\frac{\beta}{\ln \mu}\right) \ln\left(\frac{h-h_c}{\zeta}\right)$ , while for large values ( $\frac{h-h_c}{\zeta}$ ) the oscillations are damped as  $\frac{(h-h_c)}{\Lambda(h)} \rightarrow 0$ . In Figure S3 in the Supporting Information, we plot Equation (4) to evidence the increasing trend with overlapped oscillations then decaying to a plateau when  $h > \zeta$ . Hence, we fix  $\sigma_0$ ,  $a_0$ ,  $h_c$ ,  $\zeta$ , and  $\beta$  according to best-fit values obtained from Equation (3), then we fit the experimental data with three parameters ( $f_1 = \frac{1}{\ln \mu}$ ,  $a_1$ , and  $\varphi_1$ ) for one wave expansion, and five parameters ( $f_1$ ,  $a_1$ ,  $a_2$ ,  $\varphi_1$ , and  $\varphi_2$ ) for two waves. We also explored one wave fit where  $a_0$  and  $\zeta$  were released. The best-fit parameters are reported in Table S1 in the Supporting Information and the best-fit curves Equation (4) are shown in Figure 3 (blue line with one wave, green with one wave and extra free parameters, orange with two waves). All oscillations exhibit two distinctive features: i) their period stretches once the thickness is above the critical thickness  $h_c$ , and ii) their amplitude increases across the thickness range. As no damped oscillations are produced, we infer that the range of thicknesses explored lies below  $\zeta$ . However, the experimental data exhibit significant deviations from the prediction of Equation (4): in all the fitting curves, several peaks are out-of-phase with roughness oscillations; high-frequency ringing appears near the transition (these small oscillations, however, may be convolved beneath the second peak from 4.5 to 6 nm); the phase shift with respect to the experimental data is more sizable near the transition  $h \approx h_c$  (where the theoretical prediction should instead being more accurate) and for the large oscillations.<sup>[42]</sup>

### 2.3. Description of Roughness Oscillations by Local Waves

In search of a more quantitative description, we argue that the presence of a single critical point may be the limiting assumption. Therefore, we propose that the observed trend is the result of multiple transitions, each leading to a local oscillation, no longer bound to the original transition  $h_c$ . Hence, we introduce, in addition to the wavelength  $\lambda(h)$ , the center of the local oscillation,  $\eta_c(h)$  that we suppose to vary as a function of thickness  $h$ . In Section 2.5, we detail how  $\lambda(h)$  and  $\eta_c(h)$  were determined. The expression then reads

$$\sigma(h) = \sigma_0 + \left[ 1 - \exp \left[ - \left( \frac{h-h_c}{\zeta} \right)^\beta \right] \right] \cdot \left[ a_0 + \sum_{m=1}^{\infty} a_m \sin \left( 2\pi \cdot m \cdot \left[ \frac{h-\eta_c(h)}{\lambda(h)} \right] + \varphi_m \right) \right] \quad (5)$$

In our fit, we retain only the first local wave,<sup>[42]</sup> to keep the number of fitting parameters to a minimum (free variables are  $a_1$  and  $\varphi_1$ , all other parameters are kept fixed from the best fit Equation (4)). The best fit with Equation (5) is the red line in Figure 3. It is apparent how all oscillations are properly mapped both in amplitude and in phase.

### 2.4. Analysis of the Correlation Lengths

We analyze now the linear power spectral density versus wavevector  $k = 2\pi/x$  ( $x$  being the lateral length scale) to extract three correlations lengths  $\xi_n$  ( $n = 1, 2, 3$ ) from the intersections  $k_n$  ( $n = 1, 2, 3$ ) between adjacent power-law scaling segments (linear in double log scale) with different slopes, since  $\xi_n = 2\pi/k_n$ . The method is summarized in Figure S4 in the Supporting Information. The correlation lengths relate to the interisland distance ( $\xi_1$ ), the island size ( $\xi_2$ ), and the exposed terrace width ( $\xi_3$ ). Their mean values ( $\pm$  standard deviation) are 1.96 ( $\pm 0.87$ ), 0.47 ( $\pm 0.16$ ), and 0.16 ( $\pm 0.04$ )  $\mu\text{m}$ , respectively, as evidenced in Figure S4c in the Supporting Information where they are superimposed to the corresponding features in the AFM images. Interestingly, the correlation lengths versus  $h$  (see Figure S7, Supporting Information) oscillate in phase, consistently with the “ringing” between small/close and large/far islands in the sequence of AFM images in Figure 1b–o. In past reports,  $\xi_1$  versus  $h$  was shown to decay to a constant plateau above the roughening transition.<sup>[5]</sup> Again, oscillations are seamless and there is no evidence of the roughening transition.

We focus on the larger correlation length  $\xi_1$ . In Figure 3b, we overlay the evolution of  $\xi_1$  with that of  $\sigma$  to evidence the antiphase correlation of the oscillations of  $\xi_1$  with those of  $\sigma$ , viz., maximum  $\sigma$  or  $\xi_1$  corresponds to minimum  $\xi_1$  or  $\sigma$ , as evidenced by double tip arrows. Hence, a parametrization as Equation (5) (deprived of the exponential increasing trend) may be adequate to describe the evolution of  $\xi_1$ . For the first-order component would read as

$$\xi_1(h) \approx \xi_{0,1} + b_1 \sin \left( 2\pi \left[ \frac{h-\eta_c(h)}{\lambda(h)} \right] + \phi_1 \right) \quad (6)$$

where the zero-frequency component  $\xi_{0,1}$  is the mean value across the  $h$ -range. Equation (6) expresses the fact that depending on the value of  $\phi_1$ , the correlation length  $\xi_1$  should scale versus the thickness-dependent (dimensionless) angular frequency  $\frac{h-\eta_c(h)}{\lambda(h)}$  either linearly for  $(\phi_1 - \varphi_1) \rightarrow \pi$ , or superlinearly when  $(\phi_1 - \varphi_1) \rightarrow \pi/2$  for small values of  $\frac{h-\eta_c(h)}{\lambda(h)}$ . This is confirmed by the plot of the correlation length and the angular frequency versus  $h$  in Figure 3c, where  $\frac{h-\eta_c(h)}{\lambda(h)}$  and  $\xi_1$  clearly follow each other.

### 2.5. Quantization of the Wavelengths

We explain how we parametrized  $\lambda(h)$  and  $\eta_c(h)$  in Equation (6) from the experimental data. Oscillations were numbered as integers  $n$  from 1 to 7, according to the sequence of maxima/minima exhibited by the roughness. Then, we extracted the functional dependence of the period  $\lambda$  versus  $n$  by taking  $\lambda_{\max(\min)}$  (red empty upward (downward) triangles in Figure 4 left axis) as the distance between adjacent peaks (valleys) of the roughness, e.g., from a maximum (a minimum) experimental data point to the next one. We define the mean local wavelength as  $\langle \lambda \rangle = \frac{\lambda_{\max} + \lambda_{\min}}{2}$  (full red circles in Figure 4). Surprisingly, the oscillations exhibit a *discrete set of wavelengths*, thereby giving rise to a stepwise behavior of  $\langle \lambda \rangle$  ( $n$ ) which we describe with the linear combination of step functions

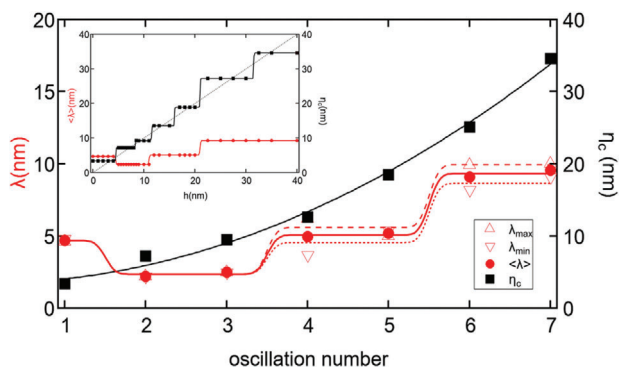


**Figure 4.** Quantization of the local waves: wavelength  $\lambda$  (left axis, red symbols) and center of oscillation  $\eta_c$  (right axis, black squares) versus the oscillation number (counted from the sequence of either the maxima or the minima of roughness, starting from  $h > 0$ ); red symbols are wavelengths estimated as distance between adjacent maxima (empty upper triangles), minima (empty lower triangles), and mean wavelength (solid circles). Inset: parameterized mean wavelength  $\langle \lambda \rangle$  (left axis, red circles) and center of oscillation  $\eta_c$  (right axis, black symbols) versus thickness  $h$ . Continuous lines are best fit with linear combination of step functions.

(in curly brackets) in Equation (7)

$$\lambda(n) = \frac{1}{2} \sum_{m=0}^4 \lambda_m \cdot \left\{ 1 + \operatorname{erf} \left[ \frac{(n - 2 \cdot m + \epsilon)}{\sqrt{2} \cdot \delta} \right] \right\} \quad (7)$$

where  $\operatorname{erf}(x)$  is the error function,  $\epsilon = 0.5$  is the (arbitrary) smearing of the step,  $\delta = 0.1$  is the (arbitrary) broadening of erf, the plateau values are  $\lambda_0 = 4.8$  nm,  $\lambda_1 = -2.4$  nm,  $\lambda_2 = 2.4$  nm,  $\lambda_3 = 4.8$  nm,  $\lambda_4 = 9.6$  nm. The wavelengths are  $\lambda(1) = 4.8$  nm,  $\lambda(2) = \lambda(3) = 2.4$  nm;  $\lambda(4) = \lambda(5) = 4.8$  nm thus, the wavelengths are integer multiples  $\kappa_n = 1, 2, 4$  of 2.4 nm. The minimum step value approximately matches the nominal thickness of 1.5 ML of pentacene, hence 1.5, 3, and 6 ML thick layers are involved in the transition from rough to smooth film (and vice versa).

We take the center of the  $n$ th oscillation  $\eta_c(n)$  as the mean thickness between the thickness of adjacent maximum and minimum of the roughness:  $\eta_c(n) = \frac{h_{\max,n} + h_{\min,n}}{2}$ . The trend of  $\eta_c(n)$  versus oscillation number  $n$  is shown in Figure 4 right axis. The solid black line in Figure 4 right axis is the best fit parabola branch  $\eta_c(n) = \eta_0 + \eta_1 \cdot n + \eta_2 \cdot n^2$  describing the shift of the oscillation centers.

We then transform the oscillation wavelength  $\langle \lambda \rangle(n)$  and the center  $\eta_c(n)$  into thickness-dependent functions  $\langle \lambda \rangle(h)$  and  $\eta_c(h)$ . We assign each experimental thickness value  $h$  to the oscillation number  $n$  when  $h$  falls within the  $n$ th oscillation, viz.,  $h \in [\eta_c(n) - \langle \lambda(n) \rangle / 2; \eta_c(n) + \langle \lambda(n) \rangle / 2]$ . The results are shown in the inset of Figure 4. Again, a linear combination of step functions allows us to fit  $\langle \lambda \rangle(h)$  and  $\eta_c(h)$  as a continuous function that we input it into Equation (5). The fitting with Equation (5) reproduces all oscillations and phases above  $h_c$ . When the thickness values are shared by two local oscillations, dimples and glitches artifacts appear in the red line of Figure 3a.

## 2.6. Correlation between Morphological Oscillations and Transconductance

We finally assess the effect of the morphological oscillations on the electronic properties of the organic transistors operated both in air and in electrolyte. The electrical measurements are carried out in the same devices used for the previous morphological analysis. Representative transfer characteristics for OFETs and electrolyte-gated OFETs (EGOFETs) are shown in Figure S5 in the Supporting Information, while typical output characteristics for OFETs and EGOFETs are shown in Figures S11 and S12 in the Supporting Information, respectively. We focus on the transconductance  $g_m$ , which is the derivative of the channel current with respect to the gate voltage  $V_{GS}$ . This parameter quantifies the amplification capability of the OFET or, in other words, its potentiometric sensitivity (i.e., the variation of the transistor channel current in response to a variation of the gate potential). Transconductance is a critical parameter in EGOFET-based biosensors, where recognition events cause a small shift of the gate interfacial potential which shall be transduced in a high channel current variation. We extract  $g_m$  from the transfer curve and plot the evolution of its largest value (the one corresponding to the linear regime) versus  $h$  in Figure 5a for OFET and Figure 5b for the EGOFET. The onset of the transconductance appears at the peak of the first oscillation at about 3 nm, thus confirming that, similarly to previous reports, the percolation of charge carriers requires the pentacene domains to form an interconnected layer.<sup>[13]</sup> Detail of a topographic AFM image between the SiO<sub>2</sub>/Si channel and the gold electrode with a 3 nm pentacene thin film is shown in Figure S6 in the Supporting Information.

The initial  $g_m$  increases by two orders of magnitude at the first few nm (see logarithmic plot of  $g_m$  versus  $h$ , in Figure 5b and Figure S8a,b, Supporting Information) then the oscillations in the range of one order of magnitude start to appear. If we consider a thickness invariant capacitance, then the main contribution to the variations of the transconductance is from the charge carrier mobility. The conversion of  $g_m$  into charge carrier mobility  $\mu$  yields for our pentacene OFETs values of  $\mu$  on the order of 0.1 cm<sup>2</sup> V<sup>-1</sup> s<sup>-1</sup> for the maxima and 0.01 cm<sup>2</sup> V<sup>-1</sup> s<sup>-1</sup> for the minima. The upper limit is one order of magnitude smaller than best values reported for pentacene thin-film transistors.<sup>[43–45]</sup> The  $g_m$  oscillations are correlated to the ones of  $\sigma$  and  $\xi_1$ , with the smooth thin films exhibiting the maximum transconductance and the rough thin films exhibiting the minimum transconductance. The fact that transconductance oscillates around a mean value of 7  $\mu$ S indicates that the wetting/dewetting transitions do not (else, they only partially do) involve the charge transport layer “buried” at the bottom of the channel. It is then clear that the oscillation observed in  $g_m$  must involve mostly the upper layers above the buried transport channel that are dynamically involved in the transitions. Because of it, we infer that the enhancement of transconductance in the wetting stage of growth may be re-conducted to the addition of active layers for charge carrier accumulation and transport.

This explanation hints that the Debye length of the transversal field exceeds the few monolayers limit that was initially postulated on the basis of low values for the dielectric permittivity.<sup>[46]</sup> There could be other more subtle effects due to the matching of the upper layers with the domain below, leading to recrystallization or boundary healing or bridging, and consequent

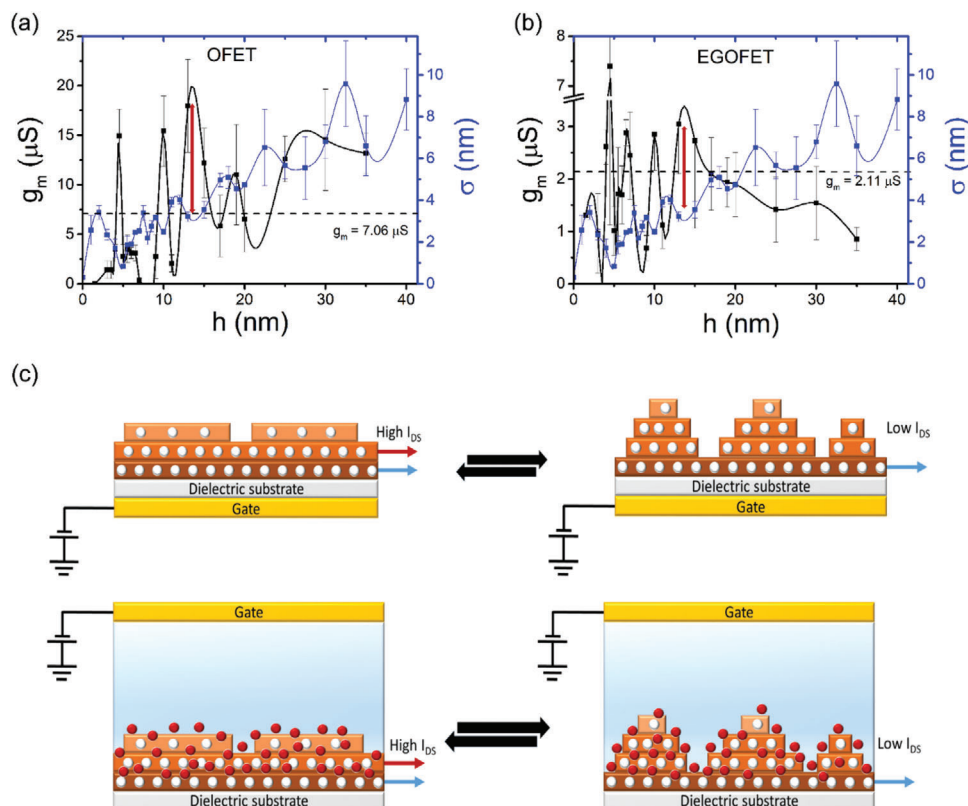


**Figure 5.** Transconductance  $g_m$  (left axis, black) and roughness  $\sigma$  (right axis, blue) versus the thickness  $h$  of a) OFET and b) EGOFET. The continuous black and blue lines are guides to the eye. The horizontal black dashed lines indicate the positions of the mean transconductance values. The red arrows points at highlighting the antiphase relation between maximum  $g_m$  and minimum roughness, as the oscillating behavior of the  $g_m$  versus  $h$ , specifically the antiphase relation of  $g_m$  with  $\sigma$  and the consequent in-phase relation with  $\xi_1$  c) Drawing illustrating the proposed mechanism for the accumulation and transport of charge carriers (white dots) in the OFET. In both wetting (left) and dewetting (right) morphologies, the gate electric field generates carriers across both bottom layers (brown) and upper layers (orange). The bottom layers (brown) remain unchanged and connected in both morphologies. In the wetting morphology, the upper layers are connected and provide conductive pathways for the charge carriers to transport current. In the dewetting morphology, the upper layers are not connected and cannot effectively transport current. As thickness increases, both the thickness of the bottom and upper layers increase, giving rise to the oscillations with increasing wavelength and amplitude, both length scales being related to the thickness of the dynamic upper layers. The black arrows indicate the recurrence of the transitions in both directions. d) Drawing illustrating the proposed mechanism for the accumulation and transport of charge carriers (white dots) in the EGOFET. The blue region indicates the electrolyte, with anions evidenced as red circles, whereas cations that accumulate to the gate/electrolyte interface are not shown.

more efficient transport pathways. Along these lines, the rough stage of growth may lead to the minimum transconductance because there are fewer active layers available (only the ones of the buried layers sustain the current), else the small islands may affect the polarization that accompanies charge carriers, hence slowing them down by a greater effective mass. In addition, in this case, a re-crystallization into smaller domains may lead to a detrimental effect on the transconductance, as it enhances energy disorder in the buried channel underneath.

A similar oscillating behavior is also observed in EGOFET (Figure 5b). In the presence of the electrolyte, the gating mechanism involves the gate-driven accumulation of anions at the interface between the electrolyte and the pentacene film. The oscillations due to the iterated smoothing/roughening phenomenon clearly influence also the transconductance of the EGOFET. More specifically, the devices with the highest transconductance, which correspond to 6, 11, 15, and 19 nm pentacene thin films, exhibit large islands and small roughness morphology suggesting that both upper and lower layers contribute to the conductance chan-

nel. As charge transport pathways are to be continuous, the modulation of the morphology bottom layers hints to a substantial degree of ion penetration in the semiconductor thin film, at variance with the simplest picture of interfacial capacitive interaction between ions and carriers across the basal plane of pentacene. The result is that the contribution of the upper layers to the current adds up in parallel to the one from the buried channel and the transconductance tends to increase. This is not immediately intuitive, since—in principle—the smaller surface area of the smooth pentacene films would correspond to a smaller effective gating capacitance. Nonetheless, it is clear from the present investigation that continuous pathways that involve a greater number of pentacene monolayers in the smoother films facilitate charge transport, leading to the increased charge-carrier mobility and to the maximization of transconductance for smooth films. Also in this case, if we assume the capacitance for the electrical double layer constant and equal to the value  $14.6 \mu\text{F cm}^{-2}$ ,<sup>[47]</sup> the charge carrier mobility  $\mu$  undergoes one-decade oscillations from  $0.005 \text{ cm}^2 \text{ V}^{-1} \text{ s}^{-1}$  maximum to  $0.0005 \text{ cm}^2 \text{ V}^{-1} \text{ s}^{-1}$  minimum.

### 3. Discussion

We first discuss the physical meaning of the antiphase oscillations of the roughness and correlation length in terms of wetting/dewetting transitions.<sup>[48–50]</sup> Cues of dewetting were present in the morphology discussed in Figures 1 and 2. We pick upon the definition of dewetting as the “spontaneous rupture of a continuous smooth (wetting) film.” The analogy leads us to associate the minimum  $\xi_1$  and maximum  $\sigma$  to a dewetted film (viz., made of islands which are close/small/tall (*pyramid*) as schematically depicted in Figure 5c top), whereas maximum  $\xi_1$  and minimum roughness to a wetting film (viz., made of islands distant apart/large/low (*ziqqurat*), depicted in Figure 5c bottom). The prototypical morphologies in Figure 1 are easily recognized (for instance Figure 1h,i for dewetting and wetting, respectively). The antiphase relationship between correlation length and roughness is conserved across the whole thickness range, which strongly indicates the iteration of wetting/dewetting transitions upon growth. Interestingly, there are no solutions of continuity along the thickness neither evidence of the roughening transition. The oscillations remind of a coherent phenomenon with a long-range memory and adaptivity. The adaptivity is evidenced by the increase of the relevant film thickness, which we identify with  $\langle \lambda \rangle$  versus  $h$  stepwise from 1.5 to 3 to 6 ML, as shown in Figure 4 inset. This discrete behavior hints us to associate the minimum thickness 2.4 nm  $\cong$  1.5 ML of pentacene, to a “roughening quantum” or “quantum of instability.” Thus, the growing film can be regarded as dynamically oscillating versus thickness between two states, a rough and a smooth one, with a period  $\langle \lambda \rangle$  equal to one, two, four times the quantum of instability depending on the total film thickness  $h$ .

We now examine the relationship between our interpretation of the quantized phenomenon and the continuous theories of dewetting.<sup>[48]</sup> According to the latter, the lateral characteristic length scale of dewetting (here associated with the interisland distance  $\xi_1$ ) would scale versus thickness  $h$  as a power law

$$\xi_1 \approx \xi_c \cdot (h/t_c)^q \quad (8)$$

where the exponent  $q = 2$  would identify spinodal dewetting.<sup>[51]</sup> The length scale  $\xi_c$  yields the proper physical dimension, which accounts for the zero-frequency component of Equation (8) upon the series expansion appropriate for the phase. Equation (8) holds for the unique wetting/dewetting transition occurring in a film whose thickness  $h$  is smaller than the critical thickness  $t_c$ . Looking at Figure 3b, one notices that the oscillating behavior of  $\xi_1$  does not obey Equation (8). To reconcile our evidence with the theoretical description of dewetting, we identify  $t_c$  with the wavelength  $\langle \lambda \rangle(h)$  and the thickness of the dewetting film with  $h - \eta_c(h)$ . In this manner, we introduce the thickness dependence on the relevant length scales in Equation (8) that now reads

$$\xi_1(h) \approx \xi_c \cdot [(h - \eta_c(h)) / \langle \lambda \rangle(h)]^q \quad (9)$$

Equation (9) qualitatively accounts for the correlated trends shown in Figure 3c, where each peak in the correlation length matches the position of the peaks of the angular frequency. The quantitative assessment of the value for the exponent  $q$ , that would allow us to assign the phenomenon to a mechanism of

dewetting, requires a more quantitative extraction of  $\xi_1$  which goes beyond the scope of this work. However, it is important to highlight that since  $|h - \eta_c(h)|$  is lesser than the whole thickness  $h$  (see inset of Figure 4, where the dashed diagonal line represents the values  $h$ ), hence only the upper layers undergo dewetting, whereas the bottom layers remain unaffected.

Our evidence that both the density and charge carrier mobility are strongly affected by the wetting or dewetting morphologies strongly supports the scenario where the upper layers in the wetting morphology are populated by the gate-induced charge carriers and thereby transported. This is schematically illustrated in Figure 5c,d. For the OFET Figure 5c, this occurrence implies the penetration depth of the Debye screening length of the gate electric field across the pentacene film is larger than the one expected from previous models (a few nm).<sup>[46]</sup> Similarly, in the dewetting morphology, charge carriers generated in discontinuous upper layers are not mobile and contribute no extra current to that transported in the bottom layer.

The EGOFET requires a different explanation. In the common EGOFET picture, the anions accumulate at the basal plane, and hence “electrostatically” dope the layers exposed to the electrolyte. This would make more favorable for the anions to interact with the upper layers, where the dewetting morphology yields a larger electroactive surface area with the terrace edges and basal plane. The one-decade oscillation of the transconductance, with maxima once again exhibited by the wetting morphologies clearly show that both the connected upper and bottom layers in the wetting morphology, or the bottom layers only in the case of the dewetting morphology, are at reach for anions. This means that anions penetrate the whole volume of the channel, in analogy with the scenario invoked for organic electrochemical transistor. Indications of volume penetration in P3HT channels was provided by means of electrostatic force microscopy.<sup>[52]</sup> Our work clearly shows that ion penetration occurs also in molecular semiconductors, like pentacene that forms ordered domains by crystal packing. We cannot sort out whether ion penetration occurs through vacancies and defects, else involves diffusion in between the herringbone structure of pentacene. This opens a more complex scenario compared to the standard capacitive coupling through the electrical double layer formed by the electrolyte at the interface with the pentacene channel that deserves a deeper investigation in future.

#### 3.1. On the Kinetic Origin of the Wetting/Dewetting Transitions

The discovery of a novel growth mode characterized by iterated wetting/dewetting transitions involving an increasing number of monolayers, forming the upper layers, which reorganize dynamically, opens fundamental questions on the growth mechanisms through which the ruptured/healed film keeps memory of the previous transitions and transmits it to the upper layers. Therefore, we discuss a possible origin for the observed phenomenon based on a molecular view and kinetic arguments, because of the inherent nonequilibrium of high vacuum growth. The first oscillation on the hexamethyldisilazane (HMDS)-terminated silicon oxide substrate first the pentacene film dewets/roughens (at 3 nm), then wets/smoothens (at  $\approx$ 5 nm). In this early stage, the transition can be regarded as the 2D filling of the substrate



area with 3 ML thick islands originated by 3D nuclei due to the combination of temperature and rate in the “dynamic phase diagram” of nucleation (see ref. [35]). After the first smoothing, the subsequent rough/3D growth seems to obey the action of the Erlich–Schwöbel’s barrier, which by preventing downward flux of molecules from the growing terraces effectively yields a larger upward flow and a faster out-of-plane growth rate. The unexpectedly rapid (on the nm thickness change) smoothing could be consequence of kinetically re-balancing of the fluxes with the eventual dominance of the downward flux that leads to smoothing. Effectively, this phenomenon hints the apparent collapse of the Schwöbel barrier, and/or the increased lateral diffusivity of the impinging molecules at half of the “quantum of instability.” The former is not easily explained unless invoking local reconstruction of the terrace edges. The latter may be reconducted to an effective temperature increase, which owing to the constant deposition temperature at 80 °C may be ascribed to the existence of a thermal gradient that is coverage-dependent both globally and locally. This gradient would be established both in- and out-of-plane with thicker islands colder than thinner ones. Recent reports on layered organic materials characterized by scanning thermal conductivity probe microscopy show a thermal conductivity contrast between adjacent layers with different thicknesses.<sup>[53,54]</sup> A thermal flux may indeed actuate molecules at terrace edges (thus disrupting the Erlich–Schwöbel’s barrier) to cause “melting” of the smaller 3D islands to form larger 2D islands. This mechanism reminds of an annealing process, which may be incidentally effective at 80 °C. The time scale (or their distribution depending on local morphology) for thermalization should be compared to the molecular impinging flux and the molecular in-plane diffusivities. The thermal flux enters into play when the time scale for thermalization is longer or comparable to the molecular flux. A molecule “landing” on “cold” peaky islands would be more off-equilibrium than a molecule landing on a “hot” smooth region, thus 3D growth dominated until the thermalization of the growing layer occurs. The process then restarts from the 2D layer and repeats itself. As the nominal thickness increases, the time scale for thermalization increases, hence the time/thickness difference of the oscillation between the rough and smooth film increases. Within this simple view, the iterated oscillations from rough to smooth morphologies might be explained, including their quantization by 1.5 ML and its multiples 1, 2, and 4: half-period of the oscillation should be the time (multiplied by the deposition rate  $r$ ) for thermalization. The emergence of the integer numbers should be explained at a quantitative level with models or simulations. Interestingly, the amplitude of the oscillation, viz., the difference of the roughness of two adjacent dewetted/wetted layers, matches half of the oscillation wavelength, hinting that the number of molecules contributing to the fluctuating topography must be compensated by a comparable number of molecules in order to smooth the topography.

We translate the kinetic arguments into wetting/dewetting transitions which are normally ascribed to the transition from a metastable to a more stable state due to the surface energy mismatch with the substrate. The connection requires mapping the higher local temperatures into lower surface (free) energy, and vice versa. We remark that in both states the pentacene molecules are oriented homeotropic with respect to the substrate. Pentacene has a lower (equilibrium) surface energy on the basal plane and

is more “sticky” on the long axis thus higher surface energy is at the edges. Indeed, smoother morphologies resulting from thermalization, as explained above, yield the wetting state. Conversely, when the thermalization is not attained, the surface energy is higher, consistently with the dewetted film. We may conclude that the oscillations observed in our experiment denote indeed dynamic wetting/dewetting transitions, where the growing pentacene film oscillates between two states with distinctive morphologies and electronic response. In the follow-up of this work, we will address whether the dynamics of the oscillations will be damped, and their memory lost, else, the phenomenon, already remarkable in time/thickness range, possesses much longer length scale memory features.

#### 4. Conclusion

Our observation that the growth above a wetting (dewetting) film leads to a dewetting (wetting) film points to a new spontaneous mechanism of wetting/dewetting transitions which repeat with a discrete wavelength (corresponding to 1.5 ML and discrete multiples thereof) upon the increasing film thickness. In the extensive literature of wetting/dewetting and related phenomena, the singularity of the wetting/dewetting transition has never been questioned to our knowledge. Here, we show that the singularity of the transition breaks down, as the transitions repeat themselves with similar features and with a quantized periodicity for increasing film thickness. This is likely the result of nonequilibrium conditions and nonconservation of mass that persist throughout our experiment, at variance with the equilibrium description of the surface instabilities.

Beyond the novelty of these features, and even more importantly for the implications on the transistor response, we showed that the growth mode is accompanied by anticorrelated oscillations of the transconductance in both OFETs and EGOFTs. These unequivocally reveal the extreme sensitivity of the charge transport properties of the semiconductor channel to nanoscale variation of thickness. The observation that iterated wetting/dewetting transitions lead to oscillations from high to low transconductance states (and vice versa) by one decade for nm scale variation of the nominal film thickness indicates how strong the effect of the organic thin-film roughness is on the electronic properties, and how sensitive the transistors are to minimal nm scale thickness variations, when the growth conditions which lead to the manifestation of such a phenomenon are met. These results should motivate the thin-film technology to control the morphology of the channel in organic transistor at the nanoscale, to controllably prepare the device into one of the two discrete electronic responses/states. By reversing the argument, it could be envisioned to readout the thin-film morphology, either smooth or rough, by measuring the transconductance in an in situ real-time experiment.<sup>[14]</sup> This feature preludes to the possibility to design, manufacture, and operate evolvable EGOFT devices, where long-term memory effects are transformed into long-term plasticity with potentiation (high transconductance) or depression (low transconductance). It should be also appreciated that the film thickness of OFETs and EGOFTs is a very effective technological handle for the fine-tuning of the transconductance, which establishes the sensitivity of the transducer once this is integrated in a sensing architecture like an immunoFET sensor.

One could then imagine transistors operated into an ultra-sensitive sub-ng balance and flow meters.

In conclusion, we reported a coherent long range in thickness oscillatory behavior of surface roughness, correlation lengths, and transconductance occurring in the growth of pentacene thin films at the nanoscale. We demonstrated that its features are very different from those of the universal roughening transition. We also demonstrated one-decade amplitude electronic effects for nm thickness variations. The period of the oscillations and the apparent absence of amplitude damping point to a wetting/dewetting mechanism induced by the growth process that repeats itself with no apparent solution of continuity in the thickness range explored. The iterated wetting/dewetting transitions involve an increasingly larger number of uppermost layers of the growing film. This phenomenon is a novel mechanism of wetting/dewetting transition occurring in a dynamic system with nonconserved mass. The growing film retains memory of the dewetting/wetting transition at the early stages of growth, hence propagates it coherently at larger thickness length scales. More experiments are needed to assess the length scale of the memory effect, but we do not observe damping within the first 40 nm.

To date, the onset of saturated charge carrier mobility in organic transistors was associated with the roughening transition that limits the charge carrier mobility and transconductance of the device. The present work evidences the possibility to overcome this limit by avoiding the roughening transition, through nanoscale control of the thin-film growth, and greatly enhance the charge transport in the organic thin-film transistor.

## Supporting Information

Supporting Information is available from the Wiley Online Library or from the author.

## Acknowledgements

F.B. is indebted to V. M. (Nitant) Kenkre for his teachings and many constructive discussions. The authors are grateful to Sauro Succi for his thorough reading and suggestions and to Luciano Fadiga for discussions. The authors acknowledge financial support received by European Union's Horizon 2020 research and innovation programme under the Marie Skłodowska-Curie grant agreements no. 721874 (SPM 2.0) and no. 813863 (BORGES).

## Conflict of Interest

The authors declare no conflict of interest.

## Data Availability Statement

The data that support the findings of this study are available from the corresponding author upon reasonable request.

## Keywords

dewetting, organic transistors, roughness, thin-film growth

Received: May 17, 2023

Revised: June 21, 2023

Published online: July 11, 2023

- [1] H. Sirringhaus, P. J. Brown, R. H. Friend, M. M. Nielsen, K. Bechgaard, B. M. W. Langeveld-Voss, A. J. H. Spiering, R. A. J. Janssen, E. W. Meijer, P. Herwig, D. M. de Leeuw, *Nature* **1999**, *401*, 685.
- [2] S. R. Forrest, *Nature* **2004**, *428*, 911.
- [3] F. Ciccoira, C. Santato, F. Dinelli, M. Murgia, M. A. Loi, F. Biscarini, R. Zamboni, P. Heremans, M. Muccini, *Adv. Funct. Mater.* **2005**, *15*, 375.
- [4] R. Buzio, C. Boragno, F. Biscarini, F. Buatier De Mongeot, U. Valbusa, *Nat. Mater.* **2003**, *2*, 233.
- [5] I. Tonazzini, E. Bystrenova, B. Chelli, P. Greco, P. Stoliar, A. Calò, A. Lazar, F. Borgatti, P. D'Angelo, C. Martini, F. Biscarini, *Biophys. J.* **2010**, *98*, 2804.
- [6] F. Schreiber, *Phys. Status Solidi* **2004**, *201*, 1037.
- [7] F. Dinelli, J.-F. Moulin, M. A. Loi, E. Da Como, M. Massi, M. Murgia, M. Muccini, F. Biscarini, J. Wie, P. Kingshott, *J. Phys. Chem. B* **2006**, *110*, 258.
- [8] H.-L. Cheng, Y.-S. Mai, W.-Y. Chou, L.-R. Chang, X.-W. Liang, *Adv. Funct. Mater.* **2007**, *17*, 3639.
- [9] A. Chanhom, J. Nukeaw, in *2007 7th IEEE Conf. Nanotechnology (IEEE NANO)*, IEEE, Piscataway, NJ **2007**, pp. 349–352.
- [10] S.-W. Liu, C.-C. Lee, H.-L. Tai, J.-M. Wen, J.-H. Lee, C.-T. Chen, *ACS Appl. Mater. Interfaces* **2010**, *2*, 2282.
- [11] F. Biscarini, P. Samorì, O. Greco, R. Zamboni, *Phys. Rev. Lett.* **1997**, *78*, 2389.
- [12] A. C. Dürr, F. Schreiber, K. A. Ritley, V. Kruppa, J. Krug, H. Dosch, B. Struth, *Phys. Rev. Lett.* **2003**, *90*, 4.
- [13] F. Dinelli, M. Murgia, P. Levy, M. Cavallini, F. Biscarini, D. M. de Leeuw, *Phys. Rev. Lett.* **2004**, *92*, 116802.
- [14] R. Ruiz, A. C. Mayer, G. Malliaras, B. Nickel, G. Scoles, A. Kazimirov, H. Kim, R. L. Headrick, Z. Islam, *Appl. Phys. Lett.* **2004**, *85*, 4926.
- [15] B. N. Park, S. Seo, P. G. Evans, *J. Phys. D: Appl. Phys.* **2007**, *40*, 3506.
- [16] A. Shehu, S. D. Quiroga, P. D'Angelo, C. Albonetti, F. Borgatti, M. Murgia, A. Scorzoni, P. Stoliar, F. Biscarini, *Phys. Rev. Lett.* **2010**, *104*, 246602.
- [17] R. W. I. De Boer, T. M. Klapwijk, A. F. Morpurgo, *Appl. Phys. Lett.* **2003**, *83*, 4345.
- [18] C. Goldmann, S. Haas, C. Krellner, K. P. Pernstlch, D. J. Gundlach, B. Batlogg, *J. Appl. Phys.* **2004**, *96*, 2080.
- [19] J. Y. Lee, *Appl. Phys. Lett.* **2006**, *88*, 252106.
- [20] I. P. M. Bouchoms, W. A. Schoonveld, J. Vrijmoeth, T. M. Klapwijk, *Synth. Met.* **1999**, *104*, 175.
- [21] S. Kowarik, A. Gerlach, W. Leitenberger, J. Hu, G. Witte, C. Wöll, U. Pietsch, F. Schreiber, *Thin Solid Films* **2007**, *515*, 5606.
- [22] A. Gerlach, S. Sellner, S. Kowarik, F. Schreiber, *Phys. Status Solidi* **2008**, *205*, 461.
- [23] F. Family, T. Vicsek, *Dynamics of Fractal Surfaces*, World Scientific Publishing, Singapore **1991**.
- [24] A.-L. Barabási, H. E. Stanley, in *Fractal Concepts in Surface Growth*, Cambridge University Press, Cambridge **1995**, pp. 1–18.
- [25] P. I. Cohen, G. S. Petrich, P. R. Pukite, G. J. Whaley, A. S. Arrott, *Surf. Sci.* **1989**, *216*, 12541.
- [26] T. V. Desai, A. R. Woll, J. R. Engstrom, *J. Phys. Chem. C* **2012**, *116*, 12541.
- [27] S. Chiodini, A. Straub, S. Donati, C. Albonetti, F. Borgatti, P. Stoliar, M. Murgia, F. Biscarini, *J. Phys. Chem. C* **2020**, *124*, 14030.
- [28] R. Ruiz, B. Nickel, N. Koch, L. C. Feldman, R. F. Haglund, A. Kahn, F. Family, G. Scoles, *Phys. Rev. Lett.* **2003**, *91*, 136102.
- [29] S. Verlaak, C. Rolin, P. Heremans, *J. Phys. Chem. B* **2007**, *111*, 139.
- [30] M. Rost, J. Krugg, *J. Phys.* **1997**, *7*, 1627.
- [31] S. Kowarik, A. Gerlach, S. Sellner, L. Cavalcanti, F. Schreiber, *Adv. Eng. Mater.* **2009**, *11*, 291.
- [32] D. Käfer, C. Wöll, G. Witte, *Appl. Phys. A: Mater. Sci. Process.* **2009**, *95*, 273.

- [33] A. Brillante, I. Bilotti, R. G. Della Valle, E. Venuti, A. Girlando, M. Masino, F. Liscio, S. Milita, C. Albonetti, P. D'Angelo, A. Shehu, F. Biscarini, *Phys. Rev. B* **2012**, *85*, 195308.
- [34] S. Chiodini, G. D'Avino, L. Muccioli, L. Bartolini, D. Gentili, S. Toffanin, C. Albonetti, *Prog. Org. Coat.* **2020**, *138*, 105408.
- [35] S. A. Burke, J. M. Topple, P. Grütter, *J. Phys.: Condens. Matter* **2009**, *21*, 423101.
- [36] F. Dinelli, C. Albonetti, O. V. Kolosov, *Ultramicroscopy* **2011**, *111*, 267.
- [37] S. Verlaak, S. Steudel, P. Heremans, D. Janssen, M. S. Deleuze, *Phys. Rev. B* **2003**, *68*, 195409.
- [38] F. Chiarella, C. A. Perroni, F. Chianese, M. Barra, G. M. De Luca, V. Cataudella, A. Cassinese, *Sci. Rep.* **2018**, *8*, 12015.
- [39] H. Spreitzer, B. Kaufmann, C. Ruzié, C. Röthel, T. Arnold, Y. H. Geerts, C. Teichert, R. Resel, A. O. F. Jones, *J. Mater. Chem. C* **2019**, *7*, 8477.
- [40] R. B. Campbell, J. M. Robertson, J. Trotter, *Acta Crystallogr.* **1961**, *14*, 705.
- [41] F. Biscarini, R. Zamboni, P. Samorí, P. Ostojica, C. Taliani, *Phys. Rev. B* **1995**, *52*, 14868.
- [42] D. Sornette, *Phys. Rep.* **1998**, *297*, 239.
- [43] H. Klauk, M. Halik, U. Zschieschang, G. Schmid, W. Radlik, W. Weber, *J. Appl. Phys.* **2002**, *92*, 5259.
- [44] A. A. Günther, J. Widmer, D. Kasemann, K. Leo, *Appl. Phys. Lett.* **2015**, *106*, 233301.
- [45] H. Klauk, D. J. Gundlach, J. A. Nichols, T. N. Jackson, *IEEE Trans. Electron Devices* **1999**, *46*, 1258.
- [46] G. Horowitz, *J. Mater. Res.* **2004**, *19*, 1946.
- [47] T. Cramer, A. Kyndiah, M. Murgia, F. Leonardi, S. Casalini, F. Biscarini, *Appl. Phys. Lett.* **2012**, *100*, 143302.
- [48] F. B. Wyart, J. Daillant, *Can. J. Phys.* **1990**, *68*, 1084.
- [49] P.-G. de Gennes, F. Brochard-Wyart, D. Quéré, *Capillarity and Wetting Phenomena*, Springer New York, New York **2004**.
- [50] G. Witte, K. Hänel, S. Söhnchen, C. Wöll, *Appl. Phys. A* **2006**, *82*, 447.
- [51] A. Vrij, *Discuss. Faraday Soc.* **1966**, *42*, 23.
- [52] L. Q. Flagg, R. Giridharagopal, J. Guo, D. S. Ginger, *Chem. Mater.* **2018**, *30*, 5380.
- [53] J. Epstein, W. L. Ong, C. J. Bettinger, J. A. Malen, *ACS Appl. Mater. Interfaces* **2016**, *8*, 19168.
- [54] M. N. Gueye, A. Vercouter, R. Jouclas, D. Guérin, V. Lemaur, G. Schweicher, S. Lenfant, A. Antidormi, Y. Geerts, C. Melis, J. Cornil, D. Vuillaume, *Nanoscale* **2021**, *13*, 3800.